High-Fidelity Universal Gates in the ^{171}Yb Ground-State Nuclear-Spin Qubit

J. A. Muniz,[1,*] M. Stone,[1,*] D. T. Stack,[1,*] M. Jaffe,[1] J. M. Kindem,[1] L. Wadleigh,[1] E. Zalys-Geller,[1] X. Zhang,[1] C.-A. Chen,[1] M. A. Norcia,[1] J. Epstein,[1] E. Halperin,[1] F. Hummel,[1] T. Wilkason,[1] M. Li,[1] K. Barnes,[1] P. Battaglino,[1] T. C. Bohdanowicz,[1] G. Booth,[1] A. Brown,[1] M. O. Brown,[1] W. B. Cairncross,[1] K. Cassella,[1] R. Coxe,[1] D. Crow,[1] M. Feldkamp,[1] C. Griger,[1] A. Heinz,[1] A. M. W. Jones,[1] H. Kim,[1] J. King,[1] K. Kotru,[1] J. Lauigan,[1] J. Marjanovic,[1] E. Megidish,[1] M. Meredith,[1] M. McDonald,[1] R. Morshead,[1] S. Narayanaswami,[1] C. Nishiguchi,[1] T. Paule,[1] K. A. Pawlak,[1] K. L. Pudenz,[1] D. Rodríguez Pérez,[1] A. Ryou,[1] J. Simon,[1,2] A. Smull,[1] M. Urbanek,[1] R. J. M. van de Veerdonk,[1] Z. Vendeiro,[1] T.-Y. Wu,[1] X. Xie,[1] and B. J. Bloom[1,†]

[1] *Atom Computing, Inc., 2500 55th St, Boulder, Colorado 80301, USA*

[2] *Department of Physics and Department of Applied Physics, Stanford University, Stanford, California 94305, USA*

(Received 2 December 2024; accepted 8 April 2025; published 21 May 2025)

Arrays of optically trapped neutral atoms are a promising architecture for the realization of quantum computers. In order to run increasingly complex algorithms, it is advantageous to demonstrate high-fidelity and flexible gates between long-lived and highly coherent qubit states. In this work, we demonstrate a universal high-fidelity gate set with individually controlled and parallel application of single-qubit gates and two-qubit gates operating on the ground-state nuclear-spin qubit in arrays of tweezer-trapped ^{171}Yb atoms. We utilize the long lifetime, flexible control, and high gate fidelity of our system to characterize native gates using single- and two-qubit Clifford and symmetric subspace randomized-benchmarking circuits with more than 200 controlled-Z (CZ) gates applied to one or two pairs of atoms. We measure our two-qubit entangling gate fidelity to be 99.72(3)% (99.40(3)%) with (without) postselection. In addition, we introduce a simple and optimized method for calibration of multiparameter quantum gates. These results represent important milestones toward executing complex and general quantum computation with neutral atoms.

DOI: 10.1103/PRXQuantum.6.020334

I. INTRODUCTION

Error-corrected quantum computation requires the ability to perform high-fidelity gate operations and readout on large numbers of physical qubits [1]. Toward this end, platforms utilizing individually controlled neutral atoms have recently demonstrated techniques to assemble arrays of over 1000 atomic qubits [2–4], as well as midcircuit measurement [5–10]. High-fidelity single-qubit gates with arbitrary local control have been demonstrated in atoms featuring hyperfine [10] and nuclear-spin qubits [11]. Two-qubit gates with fidelity above 99%, the most commonly cited threshold for the surface code [1], have been demonstrated in hyperfine [12,13], optical [14], and metastable nuclear-spin qubits [15].

Among the different optically trapped neutral-atom platforms, ground-state nuclear-spin qubits feature long coherence times due to a high degree of insensitivity to environmental perturbations such as trap light shifts and magnetic fields, as well as a near-infinite lifetime with respect to decay [11,16]. Compared to metastable nuclear-spin or optical qubits (which suffer from a relatively short lifetime due to trap Raman scattering) and hyperfine qubits in alkali atoms (which feature a relatively high sensitivity to trap light shifts), ground-state nuclear-spin qubits are well suited for combining high-fidelity gates with atomic rearrangement. This paradigm facilitates flexible connectivity, thereby enabling the implementation of error-correction schemes that efficiently utilize physical qubits [10,17,18].

Universal gate-based quantum computation generally consists of a maximally entangling two-qubit gate (e.g., controlled-NOT (CX) [19], XX [20], controlled-Z (CZ) [21]) and individually controlled single-qubit gates. In

[*] J.A.M., M.S., and D.T.S. contributed equally to this work.

[†] Contact author: bbloom@atom-computing.com

neutral-atom systems, such single-qubit gates can be difficult in practice for closely spaced trapped qubits. This problem has recently motivated the use of global single-qubit operations for subspace benchmarking that can characterize many important gate errors in quantum systems [13,22,23]. However, for a more accurate measurement of overall gate fidelity, individually addressable single-qubit gates allow one to use two-qubit Clifford benchmarking [24,25] that is not immune to specific errors.

In this work, we demonstrate manipulation of quantum states in the ground-state nuclear spin of ^{171}Yb atoms through individually controlled single-qubit gate operations and two-qubit operations based on sequential state-selective coherent excitation to a long-lived clock state and Rydberg state. We estimate a CZ fidelity of 99.72(3)% (99.40(3)%) with (without) postselection from two-qubit Clifford-randomized-benchmarking (CRB) experiments and a single-qubit CRB fidelity of 99.963(2)%. Using a benchmark sequence that is insensitive to single-qubit phases (relevant to situations in which such phases can be canceled between pairs of gates by using echo techniques, as in Refs. [10,13]), we infer a CZ-gate fidelity of 99.86(7)% (99.56(5)%) with (without) postselection. The combination of these spatially selective high-fidelity gates with the previously demonstrated continuous loading [2] and midcircuit measurement [8] is expected to lead to new demonstrations of quantum error correction and complex circuits among many physical qubits, as we have recently shown in Ref. [26].

Section II describes the qubit array geometry and trapping wavelengths used in this work. Section III describes our single-qubit gate scheme, calibration procedure, and performance. Section IV describes our two-qubit gate as a two-step process involving clock shelving and Rydberg excitation, with detailed discussion of error mitigation strategies, benchmarking protocols and performance, and a novel calibration procedure for multi-parameter quantum gates. Section V concludes and discusses implementation of nuclear spin qubits within a quantum computing architecture.

Appendix A describes our experimental setup and readout scheme. Appendixes B–E describe details about our 1Q and 2Q gates. Details on data analysis are discussed in Appendix F. Our best understanding of our error budget is described in Appendix G.

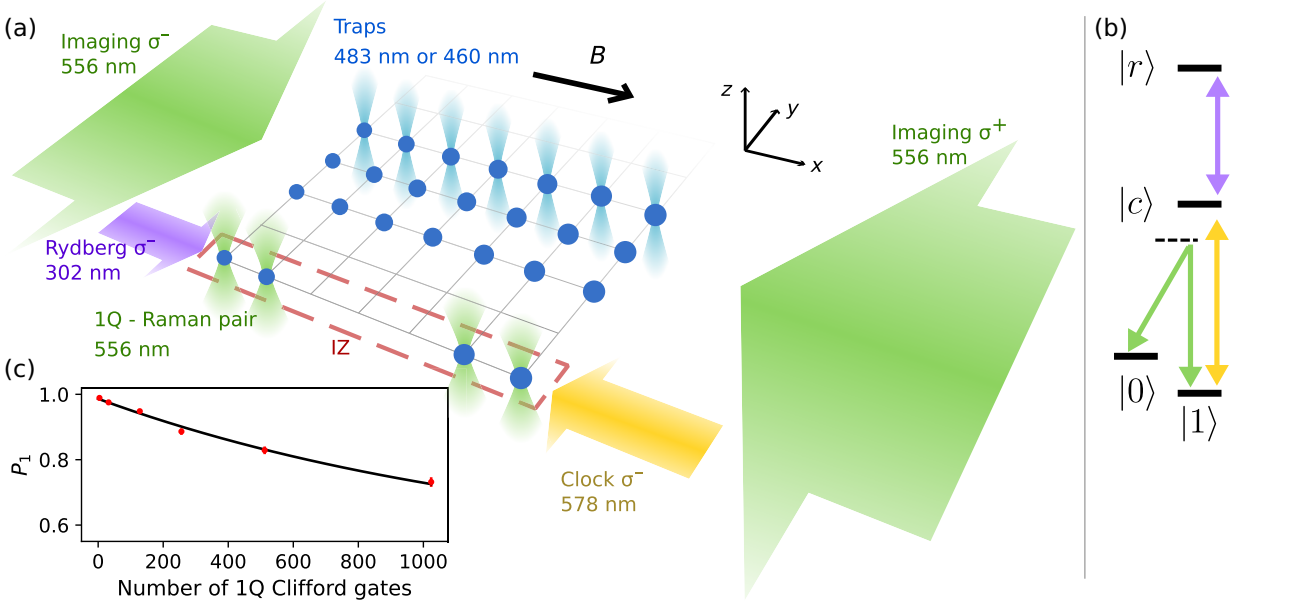

FIG. 1. (a) A diagram showing an array of trapped atoms (blue circles) and the interaction zone (red box), where spatially selective global addressing for our two-qubit gates occurs. The global addressing beams propagate along the x direction with indicated polarizations and are used for readout (green), clock (yellow), and Rydberg (purple), with their respective polarizations indicated, are shown. Individual Raman-pair beams used for single-qubit gates propagate along z and are linearly polarized along x and y, respectively. Two-qubit gates are realized simultaneously in distant atomic pairs. The magnetic field B (518 G) points along the x direction. (b) A level diagram showing the relevant transitions and atomic levels involved in our gates: nuclear-spin-qubit states $|0\rangle$ and $|1\rangle$, clock state $|c\rangle$, and Rydberg state $|r\rangle$. The virtual level for the Raman pair is shown as a dashed line. Lasers transferring population between states are shown. (c) The Clifford-randomized-benchmarking (CRB) decay averaged over the seven IZ sites. Each depth is an average over five random single-qubit (1Q) Clifford circuits and 75 repetitions of each circuit. The error bars represent the 1σ confidence interval.

II. QUBIT ADDRESSING

Our platform consists of an array of optically trapped single ^{171}Yb atoms, previously described in Refs. [2,8], where the nuclear-spin ground states $^1S_0$, $m_f = -1/2$ ($m_f = 1/2$) are used to encode the $|0\rangle$ ($|1\rangle$) states of our qubit, as shown in Fig. 1(b). In this work, we operate with a modality specifically designed to isolate the performance of gate operations. Single- and two-qubit gates are performed in the *science* optical tweezers formed with 460-nm light (which provide state-insensitive trapping for the $^1S_0 \leftrightarrow {}^3P_0$ optical clock transition used in our two-qubit gates [8,27]), while state preparation and state-sensitive nondestructive readout are performed in the *reservoir* 483-nm tweezers (which provide state-insensitive trapping for the $^1S_0 \leftrightarrow {}^3P_1$ intercombination line). In order to enhance the data rate while limiting the potential for inhomogeneity between sites, we perform two-qubit gates within one or two pairs of traps in a single row of the array, which is refilled from a larger reservoir of atoms after readout (for further details, see Appendix A). We call this row the interaction zone (IZ), as sketched in Fig. 1(a).

III. SINGLE-QUBIT GATES

The single-qubit addressing scheme employed in this work (similar to that developed in Ref. [11]) enables local and parallel control of the pulse area and phase of rotations applied to the nuclear-spin qubits of multiple atoms in the IZ simultaneously. Here, the Raman beams are red detuned by 5 GHz of the $^1S_0 \leftrightarrow {}^3P_1, F = 1/2$ transition [see Figs. 1(a) and 1(b)], resulting in a two-photon Raman Rabi rate of approximately $2\pi \times 7$ kHz. The phase of the applied gate is set by the differential phase of the two Raman beams and can be controlled arbitrarily.

The single-qubit (1Q) gate set used here consists of $Z_{\pi/2}$ and $X_{\pi/2}$ operations, where $Z_{\pi/2}$ operations are performed virtually via frame tracking and used to update the phase of the next applied $X_{\pi/2}$ pulse [28]. We characterize the performance of these gates using CRB experiments [29–31], yielding an average fidelity of 99.963(2)% per Clifford gate, averaged over the seven IZ sites. In Fig. 1(c), we show a typical averaged RB curve for seven IZ sites, with the CRB circuit executed in parallel among the IZ atoms.

Calibration of the $X_{\pi/2}$ gate requires setting the pulse area by tuning the product of Rabi rates associated with the individual Raman beams and zeroing differential light shifts by tuning the intensity ratio of the two Raman beams. For both of these calibrations, we rely on pulse sequences heavily inspired by robust-phase-estimation (RPE) methods [32]. Additionally, we perform local beam-alignment calibrations via single-beam ac-Stark shift measurements to align each set of Raman beams to the atoms [10]. Typical gate performance is limited by quasistatic drifts in alignment and beam intensities, not fundamental processes such as intermediate-state scattering. All calibrations and corrections are applied to individual qubits (see Appendix B).

IV. TWO-QUBIT GATES

Two-qubit (2Q) gates are performed by state-selectively exciting pairs of atoms to high-lying Rydberg states via a two-step process to apply a symmetric CZ gate [12]. In contrast to previously demonstrated two-photon excitation schemes, where the drive lasers are applied simultaneously and detuned from a short-lived intermediate state [12,33–35], we operate with sequential resonant excitation to and from a long-lived intermediate state [14]. This has several key advantages. It allows us to maximize the Rabi frequency to the short-lived Rydberg state given power constraints, which in turn reduces the effects of Rydberg decay. Further, by using a long-lived intermediate state, scattering from this state is reduced as well. Finally, because the excitation to the intermediate state is relatively slow, moderate differential light shifts on the narrow transition can be used to prevent atoms from participating in a gate, providing opportunities for site-selective addressing while using global gate lasers [8].

Excitation to and from the metastable clock state $|c\rangle = |{}^3P_0, m_f = -1/2\rangle$ that forms the intermediate state of our sequential excitation scheme is performed via a X_π^{clk} shelving pulse, designed and calibrated to transfer as much population as possible between $|1\rangle$ and $|c\rangle$. A combination of frequency and polarization selectivity provides state selectivity for this excitation process and thus for the two-qubit gate. From the clock state, we apply a pulse of ultraviolet (UV), 302-nm, σ^--polarized light to drive the $|c\rangle \leftrightarrow |r\rangle = |65\,{}^3S_1, F = 3/2, m_f = -3/2\rangle$ transition [see Fig. 1(b)]. The UV-pulse phase and amplitude profile are chosen to ensure that every atomic pair returns to its initial state after the pulse, while pairs of neighboring clock atoms acquire an additional π phase shift due to the Rydberg-blockade mechanism [36]. Finally, atoms are returned to $|1\rangle$ with a second X_π^{clk} pulse, having acquired a conditional phase that implements a CZ gate.

During the application of our two-qubit gates, the atoms are trapped in 460-nm optical tweezers within the IZ with a trap frequency $\omega_x/(2\pi) = 50$ kHz. Nonparticipating reservoir atoms are maintained in $|0\rangle$ and do not couple to $|c\rangle$.

A. Clock shelving

To ensure optimal performance of the two-qubit gate, it is crucial to minimize population and phase errors arising from the clock-shelving and -unshelving pulses. The clock pulses are applied to a Doppler-sensitive (single-photon) transition and are relatively slow ($\Omega_{\mathrm{clk}}/(2\pi) \approx 7$ kHz) compared to the trap frequency, making them sensitive to a specific set of errors: finite atomic temperature leads to a spread in Rabi frequencies between motional

states [37] and atoms can be coupled to other motional states of the trap. Laser-phase and amplitude noise near the Rabi frequency [38–40], as well as trap-induced decay from the clock state [41], can also degrade performance. Finally, quasistatic errors in clock laser detuning can lead to qubit phase shifts during the gate.

In order to mitigate the effects of atomic motion, we cool the atoms near their motional ground state along the direction of the clock laser. For cooling, we use three-dimensional gray molasses to cool atoms to $\bar{n} = 0.25(10)$ along the x direction [9]. With a Lamb-Dicke parameter $\eta = 0.26$, this would limit the clock-shelving fidelity to $< 99.8\%$ [42] for a single π pulse. With two clock-shelving pulses per qubit per CZ gate, clock-shelving errors would limit CZ fidelity significantly. To further reduce sensitivity to any effect that causes spread in Rabi rates, and atomic temperature, we employ shaped composite pulses (SCPs) [43]. The smooth pulse shape reduces unwanted frequency components that can induce motional-state-changing transitions and the composite pulse is designed to be robust to pulse-area errors. For a detailed error budget, see Appendix G.

There are significant drawbacks to using SCPs. Pulses are typically longer than for a square pulse, making them more susceptible to laser-frequency noise, Raman scattering, and quasistatic detunings. To minimize these effects, we have found that a Blackman-shaped $Y^{\rm clk}_{\pi/2} - X^{\rm clk}_{\pi} - Y^{\rm clk}_{\pi/2}$ pulse offers enough robustness, while balancing the impact from frequency noise [44]. We refer to this pulse as the $YXY^{\rm clk}$ pulse and from now on we will assume that the $X^{\rm clk}_{\pi}$ operation is a $YXY^{\rm clk}$ pulse. Additional effects that affect clock-shelving fidelity, but have smaller impact, can be found in the Appendixes C and G.

In Fig. 2(a), we measure the shelving fidelity of our $X^{\rm clk}_{\pi}$ pulses for atoms starting on state $|1\rangle$. Typical shelving fidelities per pulse exceed 99.85% in these conditions. Most of the error is population left in $|c\rangle$, with a smaller loss or decay to the other ground state due to Raman scattering of the 460-nm light. Each Blackman-shaped π clock pulse lasts 130 μs and is calibrated using RPE techniques. We characterize the laser-frequency noise on an optical self-heterodyne fiber interferometer setup [45] and with spin-locking atomic measurements that map laser-frequency noise into changes of atomic coherence [23,38]. The frequency range of interest spans from a few kilohertz to 20 kHz, where typical laser locks have limited gain. We find that the interferometer reports a larger frequency noise than that inferred from the atomic measurement, as shown in Fig. 2(b). We attribute this disagreement to a combination of excess acoustic noise and limitations on the noise floor of the interferometer; therefore we bound the contribution of laser-frequency noise to that extracted in the spin-locking experiments. The simulations presented in the appendixes incorporate laser-frequency noise to estimate the shelving fraction.

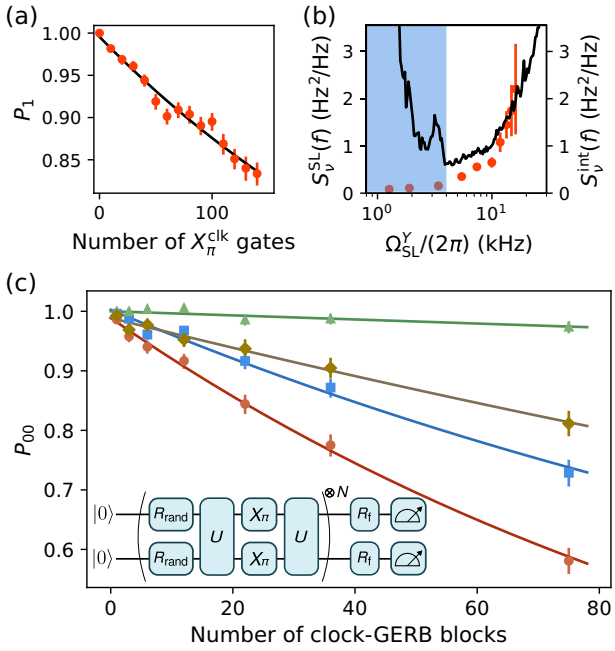

FIG. 2. Clock benchmark. (a) The probability P_1 of measuring an atom in state $|1\rangle$, after repeated application of shaped composite pulses (SCPs) $X^{\rm clk}_{\pi}$ on the IZ, for initial state $|1\rangle$. Here, we measure a 99.860(7)% shelving fraction per pulse, per atom. (b) The spin-locking measurement for the $X^{\rm clk}_{\pi/2} - Y^{\rm clk}(T) - X^{\rm clk}_{-\pi/2}$ circuit, where $Y^{\rm clk}(T)$ is a pulse along the geometrical Y axis in the $|1\rangle$ - $|c\rangle$ Bloch sphere with duration T and Rabi rate $\Omega^{\rm Y}_{\rm SL}$. For each $\Omega^{\rm Y}_{\rm SL}$, we infer the laser-frequency noise $S^{\rm SL}_{\nu}(f)$ from the temporal decay in coherence. We also show the interferometer laser-frequency noise $S^{\rm int}_{\nu}(f)$ (black). Data below 4 kHz are heavily impacted by the acoustic noise present in the interferometer (blue-shaded region). (c) Preselected (red circles), postselected on atoms remaining in the qubit subspace (blue squares), clock leakage (brown diamonds), and pair survival (green triangles) for a clock-GERB experiment ($U = X^{\rm clk}_{\pi} X^{\rm clk}_{\pi}$) measured in the two-atom basis. The solid lines are fits to $ap^x + b$, where x is the number of GERB blocks, and $b = 1/9$ for the preselected curve, $b = 1/4$ for the postselected-in-qubit-subspace curve, and $b = 0$ for the loss and clock leakage curves (see Appendix F). The error bars represent 1σ confidence intervals. The inset represents the U-GERB sequence as described in the text.

To characterize the performance of clock pulses (and, later, two-qubit gates) on arbitrary nuclear-spin-qubit states, we adopt a strategy similar to that described in Ref. [13]. This protocol consists of initializing atom pairs in $|00\rangle$ and applying N blocks each containing (i) a common random Haar-distributed 1Q rotation $R_{\rm rand}$ on both qubits, (ii) a two-qubit unitary U on the atomic pair, (iii) an echo pulse (X_π) on the qubit space, and (iv) an additional application of U, as sketched in Fig. 2(c) inset. Each block uses a different $R_{\rm rand}$ and satisfies that $U - X_\pi - U$ does not create entanglement. After the N blocks are applied, a deterministic 1Q rotation $R_{\rm f}$, precalculated under the assumption that U is ideal, returns atoms to the $|00\rangle$

state. Readout is performed in the two-qubit computational basis. By progressively constructing our CZ gate from different U gates—e.g., identity, $X_\pi^{\rm clk}X_\pi^{\rm clk}$, and finally a full CZ gate—we can identify different error sources. We call this protocol the U-global-echo randomized-benchmarking sequence (U-GERB). We note that unlike 2Q Clifford RB, this U-GERB protocol applies the same gates to atoms within a pair and so constitutes a symmetric subspace benchmark.

We measure the characteristic clock-GERB curve for $U = X_\pi^{\rm clk}X_\pi^{\rm clk}$ in Fig. 2(c). This measurement is subject to errors from the eight 1Q gates used in each block. We characterize those in the case in which U is the identity operation and measure a contribution of 0.32(2)% per atomic pair per GERB block. In this data set, characteristic of a well-tuned system, we measure a preselected fidelity for the clock shelve-unshelve sequence (red circles) of 99.80(1)% per pair, after removing the 1Q error. The post-selected fidelity of the clock shelve-unshelve sequence on atoms that remain on the qubit subspace at the end of the circuit is 99.94(2)% (blue squares), which is mostly affected by decoherence between the optical and ground-state qubits. The difference between the pre- and post-selected fidelities points to clock leakage (atoms that have remained in $|c\rangle$) and loss.

Leakage error represents population left in the clock state after each shelve-unshelve sequence (U). We are able to measure this contribution using an additional readout step preceded by a clock-repumping state, that effectively brings all of the remaining clock population back to the ground state. By estimating the fraction of pairs that are present in this readout image, compared to the image that only reveals atoms present in the qubit subspace, we determine that clock leakage (brown diamonds) contributes a 0.13(2)% infidelity in our clock-GERB sequence. Finally, using all of the readout steps, we can determine the pair-survival probability (green triangles) of 99.979(4)% after each shelve-unshelve sequence (see Appendix C).

B. Rydberg gate

Once clock shelving is complete, entangling gates are performed via the Rydberg-blockade mechanism [46], by coupling atoms from the clock state to the $|r\rangle$ state with a single global beam at 301.9 nm [Fig. 3(a)]. Our UV laser system enables Rydberg Rabi rates $\Omega_{\rm ryd} > 2\pi \times 15$ MHz, though usually a smaller Rabi rate is chosen to remain far below the Rydberg interaction energy $U/\hbar = 2\pi \times 160$ MHz. For most Rydberg operations, the 460-nm tweezers are kept on, as they provide a trapping potential for the $|r\rangle$ state due to the ion core polarizability [47] and have minimal impact on gate performance. The Rydberg-state lifetime is 65(3) μs at a typical trap depth (see Appendix D).

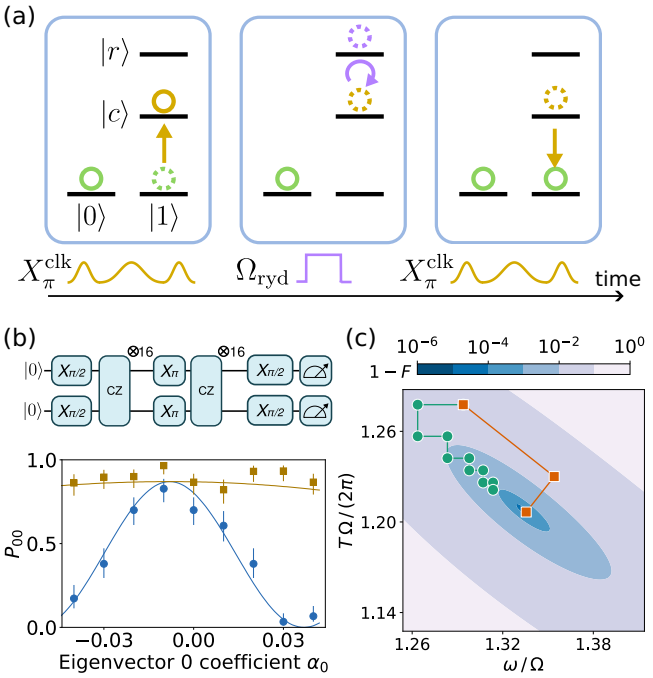

FIG. 3. The two-qubit gate. (a) A schematic depiction of the three-step gate. First, an $X_\pi^{\rm clk}$ pulse shelves qubit state $|1\rangle$ into $|c\rangle$. Second, the clock state is coupled to a Rydberg state, with the laser amplitude and phase profile chosen to implement a controlled-Z (CZ) gate. Third, an unshelving $X_\pi^{\rm clk}$ pulse transfers population from $|c\rangle$ back to qubit state $|1\rangle$. Each step is performed simultaneously on two participating atoms. (b) The CZ-gate parameters are calibrated by a series of one-dimensional (1D) scans along eigenvectors of the fidelity Hessian. After executing a circuit with repeated CZ gates (top), we measure the population in $|00\rangle$ (blue circles) and the pair survival (yellow squares). Scanning the offset α_0 along eigenvector 0 modifies the parameters $\mathbf{x} = \left(A, \omega/\Omega_{\rm ryd}, \theta, T\Omega_{\rm ryd}/(2\pi), \Delta/\Omega_{\rm ryd}\right)$ according to their respective eigenvector coefficients, $\mathbf{x} = \mathbf{x}_{\rm initial} + \alpha_0\,(0.45, -0.19, 0.14, -0.056, 0.87)$ and each variable is updated by the optimal $\alpha_{0,\rm opt} = -0.008$ multiplied by its eigenvector coefficient. This eigenvector changes $\phi_{\rm ent}$ while having little effect on survival. The solid curves are not simple fits but results from the simulation of Appendix E with fitted x offset and y scale. (c) The simulated optimization trajectory with repeated 1D scans of raw gate parameters (green circles) or eigenvector coefficients (orange squares). The eigenvector scans are decoupled and reach the minimum in a fixed number of steps, while the raw-parameter scans are not fully converged after many optimization rounds. For visual clarity, the optimization is performed over just two of the five phase parameters, ω and T. The contours represent the gate infidelity accounting only for calibration errors.

The CZ gates are implemented with an approximation of the time-optimal gate [48], using the sinusoidal phase parametrization of Ref. [13], $\phi(t) = A\cos(\omega t - \theta) + \Delta t$, with a square pulse of length T. Optimization over the phase parameters guarantees that the $|01\rangle$ ($|10\rangle$) states undergo nearly closed rotations through the $|0r\rangle$ ($|r0\rangle$) states, ideally leaving no population in the Rydberg state

and picking up a single-qubit phase ϕ_{01} (ϕ_{10}), while the $|11\rangle$ ideally leaves no population in $|W\rangle = (|cr\rangle + |rc\rangle)/\sqrt{2}$ and picks up a different phase ϕ_{11}. The latter may be decomposed into the sum of single-qubit and entangling phases as $\phi_{11} = \phi_{\text{ent}} + \phi_{01} + \phi_{10}$. Choosing gate parameters so that $\phi_{\text{ent}} = \pi$, the final unitary is $U_0 = \text{diag}(1, e^{i\phi_{01}}, e^{i\phi_{10}}, -e^{i(\phi_{01}+\phi_{10})})$, which can be converted to the ideal CZ gate $U_0 = \text{diag}(1, 1, 1, -1)$ with virtual single-qubit Z rotations.

Although optimal phase profiles are readily obtained in simulation, experimental imperfections shift the optimum, requiring calibration of the control parameters. Calibration of Rydberg gates is typically performed by a series of one-dimensional (1D) optimizations of each parameter, characterizing the phase profile of the laser drive [13]. Due to coupling between parameters, many iterations may be required to achieve convergence. We implement a simple optimized calibration by inferring the optimization landscape from the *simulated* gate to guide the *experimental* optimization. Specifically, we obtain the simulated Hessian matrix of gate performance near an optimum, diagonalize it, and then perform experimental 1D scans of gate parameters $\mathbf{x}$ along the eigenvectors according to $x_j = x_{j,\text{initial}} + \alpha Q_{jn}$, where Q_{jn} is the jth component of the nth eigenvector and α is the scan parameter [Fig. 3(b)]. Because the eigenvectors are ideally decoupled, near-optimal fidelity can be reached with a single 1D scan along each eigenvector, greatly improving the convergence compared to scans of raw gate parameters, while retaining their robustness and clarity. The principle is demonstrated through simulation in Fig. 3(c) and experimentally confirmed in Fig. 9, where eigenvector calibration produces 4 times better infidelity with 3 times fewer shots than raw-parameter scans from the same nonoptimal initial parameters. Note also the accurate prediction of the shape of each eigenvector scan in Figs. 3(b) and 8. Although simulation is not sufficient to directly predict the optimal gate parameters, the simulated Hessian is accurate enough to inform the optimization procedure and we find that it provides well-decoupled eigenvectors. Notably, the simulation need not be fine tuned with experimentally measured quantities and for these calibrations we simulate unitary evolution without incorporating measured noise, decay rates, or even laser rise times.

The gate is calibrated using an echoed metric such as the population of the desired state after applying CZ^N-X_π-CZ^N, with N gates on either side of the X_π pulse, as shown in the inset of Fig. 3(b). The echo removes any dependence on the single-qubit phases, which are obtained separately by RPE. This particular circuit enhances the sensitivity to entangling phase errors but other circuits such as GERB yield similar optimal parameters.

Finally, we point out that our gate scheme is suitable for erasure detection. To accomplish erasure detection, we note that by transferring the ground-state qubit to the metastable $^3\text{P}_0$ state for the duration of each 2Q gate, Rydberg decay, which results in the ground-state population, may be detected in the same manner as for a metastable qubit [49]. In fact, during the unshelving step, any population in the ground state will be shelved into the $^3\text{P}_0$ state and could be flagged. As shown in a concurrent publication [26], the final population in $^3\text{P}_0$ can be efficiently converted to loss, in this case by using tweezers at roughly a tune-out wavelength for $^3\text{P}_0$.

Currently, we only shelve one qubit state, which means that decay into the other qubit state will not be converted to erasure by this scheme. To obtain full erasure conversion, it would be straightforward to transfer both qubit states to $^3\text{P}_0$ before each gate, which would result in a slightly lower fidelity. However, we already observe that approximately 90% of Rydberg decay results in loss, perhaps aided by antitrapping of some states in the decay pathway at our trap wavelength.

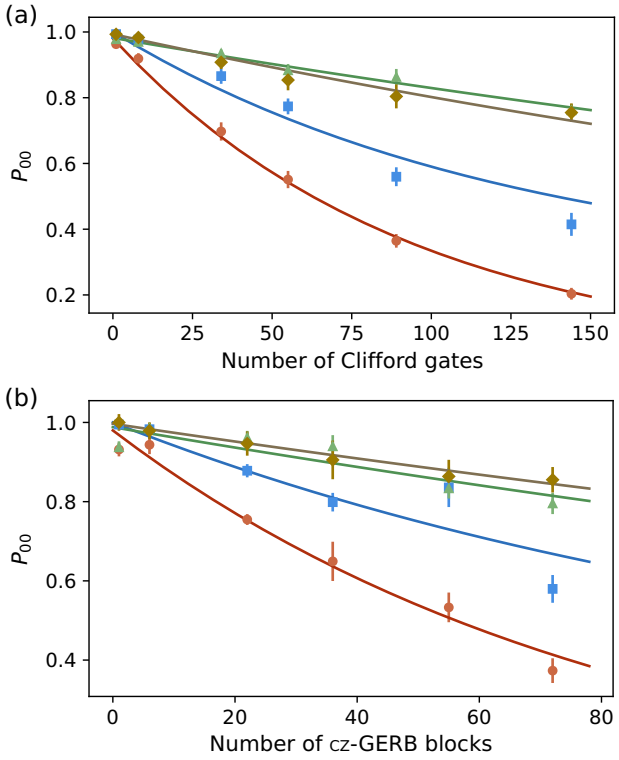

FIG. 4. Two-qubit (a) Clifford RB and (b) CZ-GERB benchmarking, showing the probability of measuring atoms in their initial state P_{00} as a function of the gate depth. The blue squares (red circles) represent the probability of returning to the initial two qubit state with (without) postselecting on atoms that are in either nuclear-spin qubit at the end of the circuit. Clock leakage (survival) measurements are shown with brown diamonds (green triangles). The solid curves are fits to the function $ap^x + b$, where x is the circuit depth, while $b = 1/4$ for the postselected-in-qubit-subspace curve and $b = 0$ for the preselected, leakage, and survival curves (see Appendix F). The error bars represent 1σ confidence intervals.

TABLE I. The infidelity contribution, the clock leakage, and the pair loss per CZ gate as measured by GERB and CRB. The clock-GERB, CZ-GERB, and 2Q-CRB infidelities are corrected by the error of a single 1Q gate and the average number of 1Q gates in each circuit.

	1Q GERB (%)	Clock GERB (%)	CZ GERB (%)	2Q CRB (%)
Preselected infidelity	0.16(1)	0.20(2)	0.44(5)	0.60(3)
Postselected infidelity	0.16(1)	0.06(2)	0.14(7)	0.28(3)
Clock leakage	0.00(1)	0.13(2)	0.12(3)	0.14(2)
Pair loss	0.00(1)	0.021(4)	0.13(3)	0.12(1)

C. Two-qubit gate benchmarking

Clifford gates are the basis for many error-correcting protocols envisioned for universal fault-tolerant quantum computation [50]. The Clifford group is sufficiently complex that most errors (even coherent errors) will be perfectly depolarized under the assumption of fixed Clifford- error channels associated with each Clifford gate. This allows one to make unbiased comparisons across different experimental platforms, even if the implementation of the Clifford operators may vary [51]. The ability to perform local and independent single-qubit operations is both important for use in quantum algorithms and allows us to perform fidelity benchmarks that average over the full Hilbert space of the qubits, as opposed to only the symmetric subspace, as has been the case in recent gate-benchmarking approaches with tweezer-trapped neutral atoms [13,15,23,52]. Physical error sources, such as decay from the Rydberg state, entangling phase, or single-qubit phase errors, will contribute to circuit errors with slightly different weights (see Appendix G) [23].

We implement two-qubit Clifford gates [30] by performing the 1Q and 2Q gates described previously. For each realization of the experiment, 20 random quantum circuits with a given depth are generated with the QISKIT EXPERIMENTS package [53] and executed 20 times per random circuit. Our measurements are summarized in Fig. 4(a). By fitting the data to an exponential decay curve, we measure an average two-qubit Clifford gate fidelity with (without) postselection of 99.40(4)% (98.93(4)%). Accounting for the average number of native 2Q and 1Q gates per Clifford gate (approximately 1.51 and 4.36, respectively), and assuming a depolarizing error model, we extract a CZ fidelity of 99.72(3)% (99.40(3)%) with (without) postselection. The atom-pair loss, the probability of losing at least one atom of the atomic pair, is measured to be 0.12(1)% per CZ gate and is dominated by Rydberg-state decoherence.

We compare this 2Q CRB measurement to a CZ-GERB measurement, which represents a symmetric subspace benchmark of our CZ gate. In this case, the presence of echoes within each GERB block (similar to the method in Ref. [13]) makes this circuit insensitive to single-qubit phase offsets and more robust against quasistatic drifts. Using the CZ-GERB circuit, we measure a fidelity of 99.86(7)% (99.56(5)%) with (without) postselection on atoms remaining in the qubit subspace. We attribute a large fraction of the difference between the fidelity metrics to quasistatic errors of the clock laser detuning, which maps into single-qubit phase errors.

The excess pair loss (0.11(3)%) measured in CZ GERB [Fig. 4(b)] relative to clock GERB [Fig. 2(c)] contributes half of the additional preselected infidelity measured between the two metrics, at 0.20(2)% and 0.44(5)%, respectively. Furthermore, the clock-state leakage is determined to be the same as that measured in our clock-GERB data set, at 0.12(3)% per gate, per pair for CZ-GERB data and 0.14(2)% for the 2Q CRB set. Additionally, errors in entangling or single-qubit phases between consecutive CZ gates will lead to excess infidelity. The observed infidelities are summarized in Table I. We provide a more detailed final error budget supported by *in situ* measurements and simulations, as well as details regarding the depth scans and fidelity extraction, in the Appendixes F and G.

V. CONCLUSIONS AND OUTLOOK

In this work, we have shown high-fidelity single- and two-qubit gates on ground-state nuclear-spin qubits. While a demonstration of two-qubit gates has been restricted to one or two pairs of interaction sites, the methods demonstrated here can also be applied to larger arrays with arbitrary connectivity by utilizing larger numbers of tweezer traps [2] and coherent movement of atoms [54], as demonstrated in Ref. [26]. These extensions benefit from the long coherence time and insensitivity to light shifts of the ground-state nuclear-spin qubit, though care must be taken to minimize atomic heating during movement. Nuclear-spin qubits also enable a complementary approach, in which the narrow linewidth of the clock-shelving transition allows the use of local light shifts to modify connectivity within static arrays of atoms (though connectivity in this approach is limited to nearby atoms). By combining these techniques with our demonstrated midcircuit measurement [8] and continuous-loading techniques [2], as well as erasure conversion provided by state-selective nondestructive measurement [49], or by state-selective trapping [26], the high-fidelity and flexible gates

demonstrated here are expected to enable the execution of complex error-corrected quantum circuits.

As part of this work, we have extensively characterized our single- and two-qubit gates, identifying key areas for improvement, such as clock-laser-quasistatic and fast-frequency noise [38,55], and further investigation of the complex Rydberg-state manifold [15,56]. The high-fidelity measured in this paper, coupled with advancements in efficient logical qubit encodings [17] and single-shot fault-tolerant schemes [57] enabled by all-to-all connectivity, place neutral-atom arrays in an exciting position in the pursuit of practical quantum computing.

APPENDIX A: SYSTEM DETAILS

Key aspects of our experimental system have been previously described in Refs. [2,8]. The lasers required to create both reservoir and science arrays and to rearrange atoms between reservoir trap sites, and the Raman beams needed for the single-qubit rotations are combined on a dichroic mirror stack. These beams are then delivered to the vacuum chamber via a high-numerical-aperture (high-NA) microscope objective (NA = 0.65, field of view = 0.5 mm). Another similar objective is placed at the other side of the vacuum chamber and is used exclusively to collect 556-nm scattered light in order to perform low-loss state-selective imaging of individual atoms. In this work, all state preparation and measurement operations are performed in optical tweezers, not a cavity-enhanced optical lattice as in Ref. [2].

The reservoir and science traps are each generated via spatial-light-modulator phase patterns [58] that are imaged on a microscope objective. The arrays used for this work consist of 84 trapping sites, distributed in 12 rows and seven columns. The top row of each array, which we call the interaction zone (IZ), is displaced from the rest of the array by 6 μm. The distance between sites in the IZ row is 3 μm. The reservoir traps have radial trap frequencies (along the x and y directions) of $\omega_{\mathrm{res}}/(2\pi) = 110$ kHz, while the science-trap frequency is $\omega_{\mathrm{sci}}/(2\pi) = 50$ kHz. Both arrays are spatially matched using camera measurements on a lower-NA monitoring system and by realizing atomic transfer experiments to calibrate any systematic offsets. To transfer atoms from one array to another, we linearly ramp up the power of one potential as we ramp down the other over 2 ms. All gates used in this work are performed in the science-array IZ, while imaging, cooling, and state preparation are performed in sites of the reservoir array at the same locations.

When atoms are initially loaded in the 483-nm reservoir traps, light-assisted collisions and optical pumping addressing the $^1\mathrm{S}_0 \leftrightarrow {}^3\mathrm{P}_1, F = \frac{3}{2}$ transition allow us to prepare single atoms in either of the two nuclear-spin ground states. State-selective readout is done by addressing the atoms for 5 ms with a single Gaussian beam propagating along the x direction (parallel to the 518-G magnetic field), with waists $(w_y, w_z) = (1.2\ \mathrm{mm}, 40\ \mu\mathrm{m})$ ($1/e^2$ radius), and σ^+ (σ^-) polarization to address qubit state $|1\rangle$ ($|0\rangle$), as shown in Figs. 1(a) and 5. As described in Ref. [8], high-fidelity state-selective readout is enabled by a large magnetic field, polarization selectivity, and the use of a magic wavelength. Typical readout has infidelity below 0.2% and loss below 0.5%.

After imaging, atoms are further cooled in the reservoir traps of the IZ to facilitate high-fidelity gate operations. In this work, we use a variant of gray-molasses cooling by addressing the atoms simultaneously with the σ^+- and π-polarized 556-nm beams addressing the $^1\mathrm{S}_0, m_F = \mp\frac{1}{2} \leftrightarrow {}^3\mathrm{P}_1, F = \frac{3}{2}, m_F = \frac{1}{2}$ transitions. The σ^+ beam is generated by the same system as the imaging beam shown in Fig. 1(a), while two π-polarized beams propagate along the y and z directions [2,9]. These π-polarized beams are circular Gaussian beams with waists of 150 μm at the atom plane. The single-photon detuning of these beams is + 2.5 MHz from the excited state, while the frequency difference between the σ^+ and π beams is equal to the qubit frequency of 389 kHz. After a cooling duration of 4 ms, we typically observe $\bar{n} = 0.25(10)$ and we do not observe significant heating or loss during the transfer of atoms between the reservoir and science arrays.

To deterministically load atoms into the IZ, we rearrange atoms with a single 483-nm tweezer created by a pair of crossed acousto-optical modulators (AODs). For

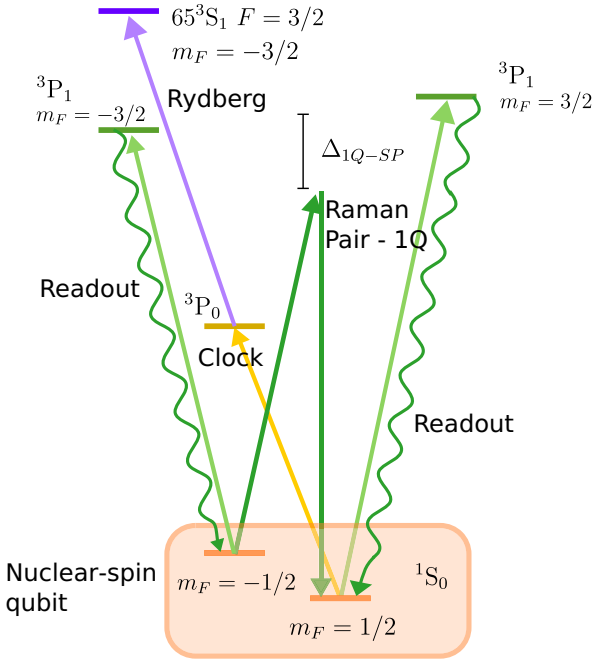

FIG. 5. A level diagram indicating the most relevant states for site-selective readout, 1Q rotations, clock shelving, and Rydberg excitation. The level spacing is not to scale.

this work, we perform CZ gates on either one or two pairs of sites in the IZ. In instances in which we load two atomic pairs, these pairs are separated by 12 μm. After the atoms are loaded, we image, cool, and prepare them in state $|0\rangle$ using global addressing. Once the atoms have been initialized, we transfer them to the 460-nm science traps. At this point, we run arbitrary circuits, e.g., GERB, Clifford RB, and RPE calibrations, as described in more detail in the following appendixes.

In a typical gate-characterization sequence in the IZ, we use several readout images with intermediate ground-state optical pumping and clock-state repumping to determine if each atom is in state $|0\rangle$, $|1\rangle$, $|c\rangle$, or lost. In particular, we take an image before starting the circuit and three images postcircuit. The second of these three images is preceded by an optical-pumping step that brings every ground state to $|0\rangle$, while the third image is preceded by a clock-repumping step that allows us to measure leakage out of the qubit subspace and lost atoms. This allows us to condition our data to successful initial pairs and determine the state of every qubit among $|0\rangle$, $|1\rangle$, $|c\rangle$, or lost. The data are analyzed in the two-qubit computational basis. We then use some of these images to properly postselect the circuit success based on some conditions or to identify population recovered by optical pumping and repumping. In this way, we can analyze errors arriving from clock leakage, loss, or anything that affects the qubit subspace.

APPENDIX B: SINGLE-QUBIT ROTATIONS

We perform arbitrary local single-qubit rotations using two orthogonally polarized Raman beams, the frequency and position of which are controlled by two pairs of crossed AODs [11]. The Raman beams are combined on a polarizing beam splitter and delivered to the vacuum chamber through a high-NA objective. At the atom plane, the beams are focused to 1.2 μm $1/e^2$ radius. One beam is polarized along the magnetic field and the other orthogonal to it. The Raman pair is detuned by $\Delta_{1Q}/(2\pi) = -5$ GHz from the $^3\mathrm{P}_1, F = 1/2$ manifold. We note that in our scheme there is a counterpropagating drive with the same two-photon Rabi rate but with a two-photon detuning of twice the qubit frequency, which sets a limit on our 1Q gate speed. However, there are a number of proposals [59] and demonstrations [60] of optimized pulse sequences to perform high-fidelity gates faster than the qubit frequency.

Upstream acousto-optical (AOM) and electro-optical (EOM) modulators enable parallel control of single-qubit operations. Calibration of the $X_{\pi/2}$ gate requires calibration of the bare qubit frequency, the differential light shift on the qubit states due to the addressing lasers, and the pulse area, as well as careful alignment of the Raman beams to the atoms. We calibrate the bare qubit frequency (near 388.9 kHz) through a 100-ms Ramsey spectroscopy experiment in the science traps, where we typically observe changes of approximately 1 Hz daily. We do not observe significant inhomogeneities in the measured qubit frequency across the IZ sites.

Calibration of the differential light shifts and the pulse area are performed by controlling the relative and common optical powers between the two Raman beams at a single site level, respectively. Inspired by RPE methods, we perform a repeated sequence of $X_{\pi/2}X_{\pi/2}X_{-\pi/2}X_{-\pi/2}$ pulses to calibrate the differential light shifts and a series of $X_{\pi/2}X_{\pi/2}X_{\pi/2}X_{\pi/2}$ pulses to tune the pulse area. We iterate these calibrations with different numbers of repetitions in order to progressively improve our precision. Raman-beam alignments are realized by mapping the ac-Stark shift of an individual beam into phase changes in a Ramsey sequence, similar to the method used in Ref. [10]. Faster camera-based measurements between the 1Q array and the trap arrays are used to correct drifts from its set point. Our single-qubit gate performance is not limited by fundamental processes such as intermediate-state scattering. Rather, based on RPE and camera-based measurements, we attribute the majority of the 1Q error to quasistatic drifts in the relative position between traps and 1Q beams. The simulations suggest that 100-nm drifts and misalignment can explain typically observed errors.

The GERB sequences for the 2Q gate rely on 1Q operations to randomize the gate of interest over a subset of arbitrary input states. Random Haar-distributed rotations are constructed from random angles ϕ_0, ϕ_1, and ϕ_2, with distributions weighted such that $R_{\mathrm{rand}} = Z[\phi_0]X_{\pi/2}Z[\phi_1]X_{\pi/2}Z[\phi_2]$ samples the Hilbert space of each qubit uniformly. At the end of the GERB sequence, we apply a single precomputed rotation $R_{\mathrm{f}} = Z[\phi_0^f]X_{\pi/2}Z[\phi_1^f]X_{\pi/2}Z[\phi_2^f]$ to return atoms to the initial qubit state, provided that U is perfect. We benchmark our GERB sequence against the 1Q Clifford RB result, by running it with $U = Id$. Each GERB block consists of four $X_{\pi/2}$ gates per atom and so eight per pair. We typically measure 0.32(2)% infidelity per GERB block (computed on an atomic pair for consistency with 2Q benchmarks), which is consistent with 8 times the average gate infidelity measured in the Clifford RB sequence. To remove the 1Q error from other GERB measurements, i.e., when U is not an idle operation, we subtract 0.16(1)% per U infidelity on each atomic pair.

APPENDIX C: CLOCK OPERATIONS

The clock beam propagates along the x direction and is elliptically shaped at the atom plane with waists $(w_y, w_z) = (400\ \mu\mathrm{m}, 35\ \mu\mathrm{m})$. The large magnetic field and polarization selectivity [see Fig. 1(a)] suppress other excitation paths and also suppress differential qubit phase shifts. We operate our clock with Rabi rates $\Omega_{\mathrm{clk}}/(2\pi)$ between 3 kHz and 15 kHz, placing us in the resolved-sideband limit with respect to the radial-science-trap frequencies

of $\omega_{\rm sci}/(2\pi) \approx 50$ kHz. In this regime, we are sensitive to both the effects of atomic motion and laser-frequency noise, which are the main contributors to the shelving error. To mitigate frequency noise seen by the atoms, we stabilize the phase of the delivered clock light via a fiber noise-cancellation setup that references the phase of the delivered light to the vacuum chamber [61]. The optical power delivered to the atoms is also actively stabilized.

We characterize the atom temperature using spectroscopy of the motional clock sidebands along x, as shown in Fig. 6(a). At typical temperatures, a single (noncomposite) Blackman-shaped pulse with a peak Rabi rate of $2\pi \times 7$ kHz shows shelving fidelities slightly above 99%, measured by repeated application of the clock pulse as in Fig. 2(a). We have verified via RPE measurements that the residual infidelity is not due to coherent errors but, rather, to the Debye-Waller effect from trapped atoms at finite temperature [42]. The use of pulse-area-robust composite pulses improves this shelving fraction, at the price of applying longer pulses with greater sensitivity to both quasistatic and time-varying laser-frequency noise. The cooling mechanism described in Appendix A has shown better clock performance while running deep circuits compared with other cooling protocols, such as Doppler cooling [8] or Raman-sideband cooling [2,16].

The lifetime of ground-state atoms in the science or reservoir traps is mostly limited by vacuum and intensity noise on the traps and is at least 5 s. However, for atoms in the clock state, Raman scattering of the 460-nm light drives population out the ^{3}P$_0$ manifold. For the science traps with a 50-kHz trap frequency, we have measured $T_1 = 1.06(5)$ s [see Fig. 6(b)]. For the $X_\pi^{\rm clk}$ SCPs used in the main text (260 μs duration), we estimate that this scattering accounts for an 0.019% error per CZ gate averaged uniformly over possible states of the atomic pair (see Appendix G). We note that such Raman scattering would act as an idle loss in metastable qubit architectures, posing a challenge with regard to achieving high-fidelity circuit operation at this trap wavelength and depth [15,35].

To measure the laser-frequency noise at 578 nm, we use a scheme similar to that described in Ref. [45]. We employ a 1 km single-mode (SM) optical-fiber interferometer surrounded by sound-absorbing material. One of the interferometer arms is frequency shifted by a 200-MHz AOM. Laser-frequency noise is mapped (via the transfer function of the delay line) into the interferometer beat note at 200 MHz, which is measured with a spectrum analyzer (SignalHound SM200B). A typical measurement is shown in Fig. 6(c). At low frequencies, the laser noise is overwhelmed by the acoustic noise present in the room [blue-shaded region in Fig. 6(c)], while we attribute the majority of the noise above 4 kHz to laser-frequency noise.

Atomic spin-locking measurements, as in Fig. 2(b), are our best estimation of the frequency noise above 1 kHz. A typical spin-locking experiment performs a Ramsey

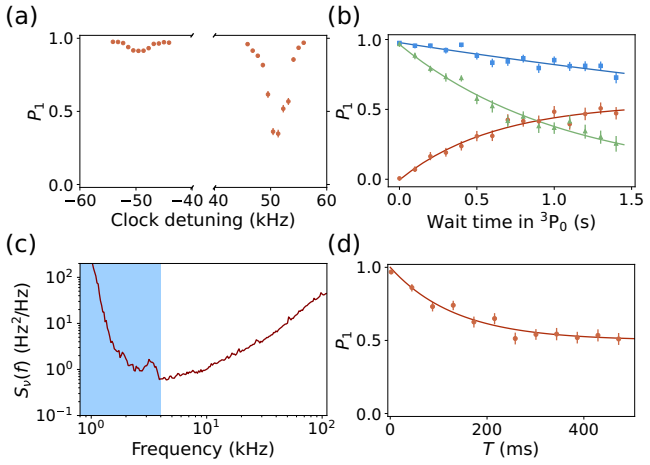

FIG. 6. (a) Sideband spectroscopy on the clock transition for atoms trapped on the science IZ (average data). (b) The clock-state lifetime. Atoms are held in the science traps (50-kHz trap frequency). We measure the population in either ground state (red circles), the atom loss (blue squares), and the population remaining in the clock state (green triangles), after holding atoms for time T. Fitted $T_1 = 1.06(5)$ s using the ^{3}P$_0$ survival data (green), while the typical loss via the ^{3}P$_2$ state and other mechanisms has a $1/e$ decay time of 5.7(6) s. (c) The clock laser-frequency noise $S_\nu(f)$ as measured in the 1-km-fiber self-heterodyne interferometer at 578 nm. The blue-shaded region represents the frequency range in which our measurement is overwhelmed by acoustic noise present in the room. (d) The coherence decay in a spin-locking experiment for $\Omega_{\rm SL}^{\rm Y}/(2\pi) = 5.5$ kHz. The fit function is $(1 + e^{-t(\Gamma_{\rm SL}+1/(2T_1))})/2$, where $T_1 = 1.06(5)$ s. The error bars represent 1σ confidence intervals.

sequence that prepares an atom along the Y axis of the optical-qubit ($|1\rangle \leftrightarrow |c\rangle$) Bloch sphere and then applies a drive with duration T and Rabi rate $\Omega_{\rm SL}^{\rm Y}$ along the Y axis [23,38]. In the presence of laser-frequency noise, the atomic coherence is displaced from the Y axis, such that a final $\pi/2$ pulse along the X axis cannot return the population to either of the poles, as shown in Fig. 6(d). From these data, we determine the $1/e$ decay rate $\Gamma_{\rm SL}$, taking into account contributions from T_1. In the linear-response approximation, the decay rate $\Gamma_{\rm SL}$ is $\Gamma_{\rm SL} = 2\pi^2 S_\nu(\Omega_{\rm SL}^{\rm Y}/(2\pi))$, where $S_\nu(f)$ is the double-sided laser-frequency noise power spectral density (PSD) [23]. We repeat this measurement for different Rabi rates $\Omega_{\rm SL}^{\rm Y}$ to reconstruct $S_\nu(f)$.

We find some disagreement between the frequency noise inferred from spin-locking measurements and that measured by the fiber interferometer, especially below 10 kHz. This may be due to unaccounted noise sources on the interferometer. For predicting the contribution of laser phase noise, we rely on the frequency PSD $S_\nu(f)$ measured by the spin-locking experiment as an upper bound to the actual laser-frequency noise.

To improve the data rate for calibrations involving our clock laser, we perform many experiments in series on

the same atoms, which can lead to leakage into the clock state. In order to recycle population from the clock state, we use a repumper on the fast $^3P_0 \leftrightarrow {}^3D_1, F = \frac{1}{2}$ 1388-nm transition. This beam propagates along the x direction and is linearly polarized. However, about 2% of the atoms that undergo a repumping cycle decay to the $^3P_2$, which is either weakly or not trapped in our tweezers, leading to loss. Therefore, before repumping, we optically pump atoms are in the ground state to $|0\rangle$, apply a high Rabi rate XY^{clk} π pulse on the $|1\rangle - |c\rangle$ transition and finally apply a resonant 1388-nm pulse to the clock state. This reduces loss significantly, speeding up relevant calibrations.

APPENDIX D: RYDBERG STATE

Our UV laser operates at 301.9 nm and is focused down to a approximately circular beam with an 18-μm beam waist, which propagates along the x direction in the IZ. We work with the $|r\rangle = |65\ {}^3S_1, F = 3/2, m_F = -3/2\rangle$ Rydberg state. Excitation to undesired m_F sublevels is suppressed by both circularly polarized light and gigahertz-scale Zeeman splitting from the large magnetic field. Recent studies of the detailed structure of the ^{171}Yb Rydberg manifold in Ref. [15] have shown that the 2Q gate fidelity can be strongly influenced by the Rydberg state used, accidental Föster resonances, or the choice of the magnetic field. We expect to further investigate this at our larger magnetic fields.

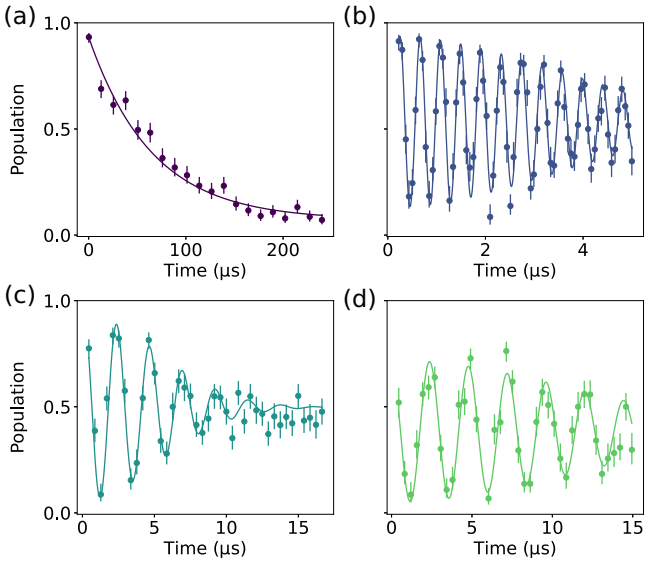

FIG. 7. Rydberg state and laser characterization. (a) Rydberg-state-lifetime measurement, by population return after a π pulse into the Rydberg state, a variable wait time, and a π pulse back. The fitted lifetime is 65(3) μs at a typical trap depth. (b) Clock-Rydberg T_2^* measurement by Ramsey decay, with a Gaussian fit of $T_2^* = 3.4(2)$ μs. (c) T_2 echo decay with traps on, Gaussian fit $T_{2,\text{echo}} = 5.1(4)$ μs. The x axis represents the total duration of the echo sequence. (d) T_2 echo decay with traps dropped, Gaussian fit $T_{2,\text{echo}} = 11(2)$ μs. The error bars represent 1σ confidence intervals.

The UV beam waist is only 18 μm and the spacing required to avoid pair crosstalk is at least 10 μm, preventing us from achieving a high UV Rabi rate in distant rows or densely populating a single row. Although we have measured the fidelity of our gates using one or two pairs, we have measured it across all possible isolated nearest-neighbor pairs in the IZ sites, or in parallel over a full row with 16 pairs in a concurrent publication [26]. We do not observe significant changes in gate fidelity, and when we do, it is mostly associated with misalignment of the single-site Raman beams.

Population and coherence decay times for the Rydberg state are shown in Fig. 7. As mentioned in the main text, the 460-nm tweezers provide a trapping potential for Rydberg atoms due to the ion core polarizability and may be kept on or dropped. The lifetime of the Rydberg state is 65(3) μs with traps on at typical depth and shows little dependence on the trap depth, so long as it is deep enough to confine the atom effectively. A Gaussian fit to Ramsey contrast decay yields $T_2^* = 3.4(2)$ μs, which is mostly explained by the UV laser phase noise, dominated by sub-50 kHz frequencies, and also reflects Doppler shifts and other slow-detuning errors. An echo sequence gives $T_{2,\text{echo}} = 5.1(4)$ μs (11(2) μs) with traps on (off), as the dephasing due to motion in the trap cannot be echoed effectively at times on the scale of the trap period.

APPENDIX E: TWO-QUBIT GATE CALIBRATION

Entangling gates implemented by transient Rydberg excitation must satisfy several constraints (accrued entangling phase and population left in the Rydberg state for each basis state) and therefore require several degrees of freedom to be tuned. The optimal values may be approximately determined by simulation but experimental model violation inevitably requires experimental calibration. In special cases, the optimal parameters can be inferred one by one from a series of experiments, as in the Pichler-Levine gate [12]. Otherwise, the conventional strategy is to parametrize the gate arbitrarily and then optimize the gate performance over 1D scans of each parameter, generally requiring multiple rounds of iteration due to coupling between the parameters.

We address this problem by simulating not just the optimal parameters but the structure of the optimization landscape. The gate performance is approximated to second order around an optimum as $I \approx I(x_0) + \frac{1}{2}\Delta x_i H_{ij} \Delta x_j$, where Δx_i is the difference of the ith parameter from its optimal value and the Hessian matrix can be determined by finite differences of I. The Hessian is well known to be useful in numerical-optimization algorithms but these algorithms are often not robust to experimental noise. We choose instead to diagonalize the

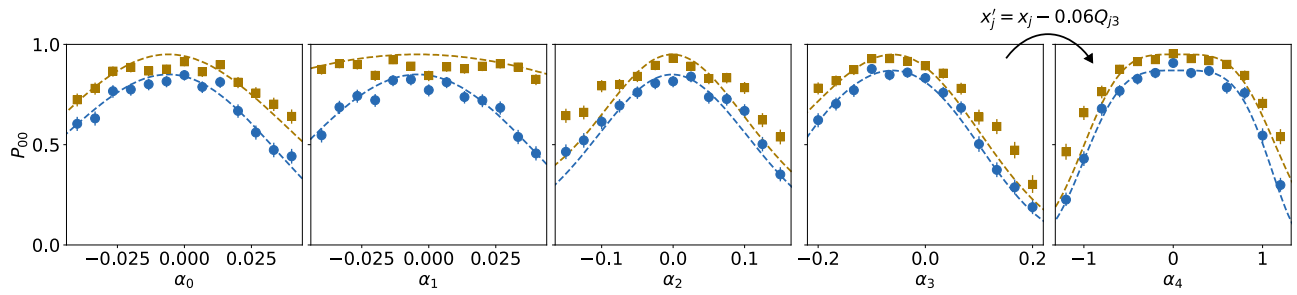

FIG. 8. Typical eigenvector scans. As in Fig. 3(b), each plot scans the offset α_n along eigenvector n, so that the raw gate parameters x_j vary as $x_j = x_{j,\text{initial}} + \alpha_n Q_{jn}$, where Q_{jn} is the jth element of the nth eigenvector. After performing the circuit shown in Fig. 3(b) (but here with only eight CZ gates on either side of the echo), we measure the population in $|00\rangle$ (blue circles) and pair survival (yellow squares). The dashed lines are not simple fits but results from the simulation of Appendix E with a fitted x offset and y scale. Here, an intentional offset from the optimal values has been introduced to eigenvector 3 before scanning, which is fully recovered after one round of scans. The gate has no quadratic dependence on eigenvector 4, leaving a strongly suppressed quartic dependence.

Hessian $\mathbf{H} = \mathbf{Q}\Lambda\mathbf{Q}^{\mathbf{T}}$ with $\mathbf{\Lambda}$ a diagonal matrix and the columns of $\mathbf{Q}$ the (orthogonal) eigenvectors of $\mathbf{H}$. Then, $I \approx I(x_0) + \frac{1}{2}\sum_n \Lambda_{nn}(\Delta q_n)^2$, where $\Delta q_n = Q_{jn}\Delta x_j$ is the scalar projection of $\Delta\mathbf{x}$ along the nth eigenvector.

Clearly, the infidelity is now a sum of decoupled functions of the Δq_n. Thus the Δq_n can be optimized independently, scanning over each by adding to $\mathbf{x}_{\text{initial}}$ a multiple of the nth eigenvector, $x_j = x_{j,\text{initial}} + \alpha Q_{jn}$, and experimentally optimizing over α, as shown in Figs. 3(b) and 8. The result, as shown via simulation in Fig. 3(c), is that the optimum may be reached with a single scan over each eigenvector. This is confirmed experimentally in Fig. 9 where, after a parameter offset is introduced to produce approximately 10% infidelity, five eigenvector scans produce a near-optimal preselect infidelity of 0.51(4)%, while 15 raw parameter scans achieve only 2.1(2)% preselect infidelity.

The gate-performance function I may be chosen as the average gate infidelity [48] of CZ-X-CZ, appropriate if optimizing in a CZ-GERB sequence that randomizes over input states, or the state infidelity for a single initial state after a sequence with multiple CZ gates, as is done in Fig. 3(b). The latter has coherent addition of entangling phase errors, magnifying the sensitivity compared to CZ GERB, which adds entangling phase errors incoherently, but the two yield similar optimal parameters. A coherent circuit leads to linear increase in precision with the number of CZ gates in the circuit [32], whereas CZ-GERB calibration circuits increase precision by the square root of the number of CZ gates. Either way, we use an echoed sequence to remove the dependence on the single-qubit phase—while the entangling phase and the Rydberg population have nontrivial dependence on the gate parameters, single-qubit phases can be easily isolated with an echo and then separately measured with RPE and corrected with virtual Z gates.

Experimental imperfections will alter the Hessian but many (e.g., finite blockade and rise time) can be easily incorporated into the simulation, and in practice the eigenvectors remain reasonably decoupled regardless. With five control parameters such as A, ω, ϕ, T, and δ, one eigenvector will have a zero eigenvalue, so only four tunable parameters are necessary to optimize a Rydberg controlled-phase (CPhase) gate. We nondimensionalize all parameters with time units by Ω_{ryd}, so that the control eigenvectors can be conveniently scaled to different Rabi rates (however, the blockade strength and rise time cannot be easily scaled in experiment, so we precompute several Hessians for different ranges of Rabi rates).

With nondimensional parameters $\mathbf{x} = \left(A, \omega/\Omega_{\text{ryd}}, \phi, T\Omega_{\text{ryd}}/(2\pi), \Delta/\Omega_{\text{ryd}}\right)$, the simulated Hessian for the circuit shown in Fig. 3(b) is as follows:

$$H = \begin{bmatrix} 663 & -9.07 & -0.00101 & 106 & 957 \\ -9.07 & 739 & -141 & 585 & -350 \\ -0.00101 & -141 & 36.9 & -121 & -0.00172 \\ 106 & 585 & -121 & 632 & -44.1 \\ 957 & -350 & -0.00172 & -44.1 & 1950 \end{bmatrix}.$$

Note the strong coupling between $\omega/\Omega_{\text{ryd}}$ and $T\Omega_{\text{ryd}}/(2\pi)$, indicated by off-diagonal elements nearly as large as the diagonal elements. This suggests that raw-parameter scans are particularly inefficient for correcting Rabi rate errors, which perturb both of these parameters, whereas eigenvector scans remove the problematic coupling.

The experimentally optimized parameters used for the benchmarking results are

$$\begin{aligned} A &= 0.733, \\ \omega/(2\pi) &= 9.72\ \text{MHz}, \\ \phi &= -0.625, \\ T &= 136\ \text{ns}, \\ \Delta/(2\pi) &= -649\ \text{kHz}. \end{aligned}$$

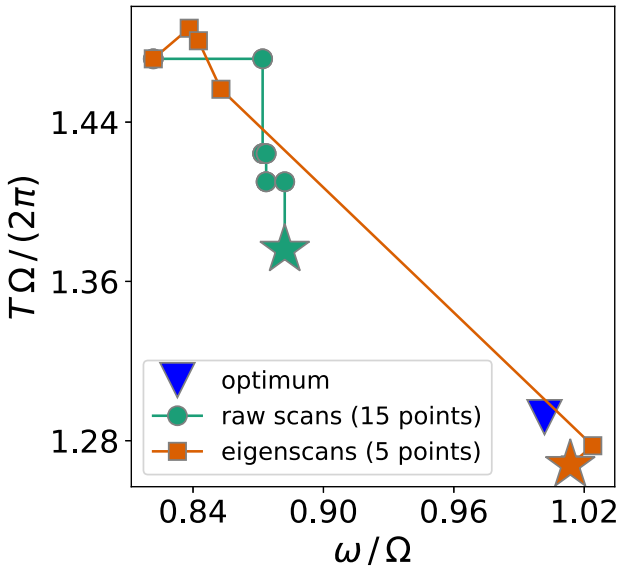

FIG. 9. An experimental optimization trajectory with repeated 1D scans of raw gate parameters (green circles) or eigenvector coefficients (orange squares), using a similar circuit to that shown in Fig. 3(b) but with only two CZ gates on either side of the echo. After initial gate optimization (blue triangle), an offset has been introduced to the gate parameters T and ω to yield an infidelity of approximately 10%. The gate has then been recalibrated with either five eigenvector scans or 15 raw-parameter scans. Note that while all raw parameters have been scanned, only changes in T and ω appear on this plot, so not all 15 points are visible. After calibration, GERB benchmarking has been performed at the parameters denoted by star markers. The eigenvector scans appear much closer to the optimum and reach a near-ideal preselect infidelity of 0.51(4)% (corrected for 0.2% error from 1Q gates), while the raw-parameter scans reach a preselect infidelity of 2.1(2)%, or 4× worse despite a 3× longer calibration procedure.

However, there is a 1D family of parameters that produce equivalent fidelity, which corresponds to moving along the zero-eigenvalue vector.

A greatly simplified simulation is used to calculate the Hessian for calibration purposes but note that a more complete model of the gate is presented in Appendix G. Here, we simulate only the unitary evolution of the gate with symmetric couplings, under the Hamiltonian

$$
\begin{aligned}
H &= H_{00} + H_{01} + H_{10} + H_{11},\\
H_{00} &= 0,\\
H_{01} &= -\Delta\,|0r\rangle\langle 0r| + \frac{\Omega_{\mathrm{ryd}}}{2}\left(e^{i\phi(t)}\,|0r\rangle\langle 01| + \mathrm{c.c.}\right),\\
H_{11} &= -\Delta\,|W\rangle\langle W| + (U-2\Delta)\,|rr\rangle\langle rr|\\
&\quad + \frac{\Omega_{\mathrm{ryd}}}{\sqrt{2}}\left[e^{i\phi(t)}\left(|W\rangle\langle 11| + |rr\rangle\langle W|\right) + \mathrm{c.c.}\right],
\end{aligned}
$$

where H_{10} is of a similar form to H_{01}, U is the Rydberg interaction strength, $\phi(t)$ is parametrized as in the main text, $|W\rangle = \frac{1}{\sqrt{2}}(|1r\rangle + |r1\rangle)$ is the symmetric one-excitation state, and the four terms H_{00}, H_{01}, H_{10}, and H_{11} act on mutually uncoupled sectors of the Hilbert space. The transformation of each qubit-subspace basis state ($|00\rangle$, $|01\rangle$, $|10\rangle$, and $|11\rangle$) under the gate is evaluated using the QuTiP Schrödinger-equation solver [62]. Loss of population left in the Rydberg state is coarsely accounted for (neglecting decay during the gate and possible decay back to the qubit subspace) by truncating the final state to the qubit subspace, consistent with the subspace-averaged fidelity of Ref. [63]. This yields a nonunitary 4×4 transformation matrix V for a single gate application. Multiple applications of the gate are modeled by repeated applications of V, which are appropriate if time is allowed for complete loss of the Rydberg population between applications, and an echoed sequence is given by $V^n\,(X\otimes X)\,V^n$.

Other than a rough estimate of the blockade strength, we do not simulate any particulars of the experiment (laser rise time, Rydberg decay rate, or decoherence) for the results presented here and we still find excellent convergence properties using the resulting eigenvectors for calibration. However, it would be straightforward to extend the simulation. The simulated Hessian could be directly used in a number of alternative optimization algorithms, potentially leading to further improvements in the calibration speed.

APPENDIX F: DATA ANALYSIS

Our two-qubit gates circuit-depth scans repeat a circuit about 20 times and sample ten different circuits for CZ GERB and 20 different circuits for 2Q CRB. The value assigned as the measured probability is the weighted average over the different circuit realizations. The error bars at each circuit depth are assigned as the standard error of the mean among the different realizations.

For the circuit-depth scans shown in Figs. 1(c), 2(c), and 4, we fit all the decay functions to exponential functions $ap^x + b$, where x represents the depth of the circuit, a and p are fitting parameters, and b is fixed to a predetermined value. Typically, b is related to the single-atom subspace dimensionality d and the total number of qubits in the measurement basis [22]. All infidelities, $1-F$, are calculated from the decay fit as

$$1 - F = 1 - \frac{(d^2-1)p + 1}{d^2} \approx (1-p)(1-b). \quad \text{(F1)}$$

Confidence intervals on the error rates and fidelities are reported based on the standard-deviation errors of the fitting parameters, taking into account the actual spread of the experimental data.

For the 1Q CRB measurement, we consider $b = 1/2$, as this is measured in the single-atom basis. For the clock-GERB experiments presented in Fig. 2(c), we choose

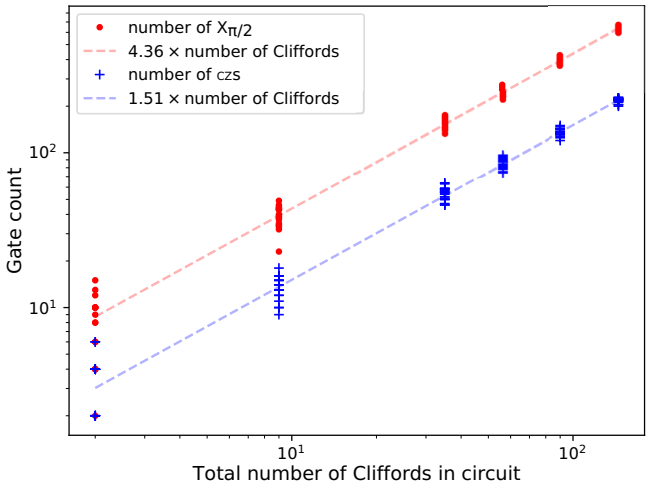

FIG. 10. The circuits used for the 2Q Clifford RB experiments, generated as random realizations of circuits with a fixed set of Clifford depths. When these are decomposed into native gates, the number of $X_{\pi/2}$ and CZ gates varies across circuits of the same Clifford depth. For the particular circuits and decomposition into native gates used here, the average number of CZ gates per Clifford gate is 1.51 and the average number of $X_{\pi/2}$ gates is 4.36.

different values of b for the different cases. For the preselected fidelity, analyzed in the two-qubit measurement basis, we fix $b = 1/9$ because each atom in a pair can be in states $|0\rangle$, $|1\rangle$, or $|c\rangle$ and leakage is larger than loss. For the postselected fidelity on the qubit subspace, each pair atom can be in states $|0\rangle$ or $|1\rangle$, so we fix $b = 1/4$. Finally, the loss measurement represents any other possibility, so we fix $b = 0$.

For the CZ-GERB and 2Q Clifford depth curves in Fig. 4, we make the choice of fixing $b = 0$ for the pair survival and preselected fidelities, but we fix $b = 1/4$ for the qubit-subspace postselected fidelity as there are four possible basis states for our readout. We set $b = 0$ in these cases because atom loss is possible and significant on both curves, and once the circuit fails to produce the desired output, the state will not go back to its initial state.

Isolating the CZ-gate error from the 2Q Clifford decay fit requires subtracting out the error incurred by 1Q gates that occur in the sequence. We do this by multiplying the known 1Q CRB error by the average number of 1Q gates in each CZ CRB sequence and dividing the remaining error by the average number of CZ gates. The average gate numbers are obtained by direct counting of the gates in the circuits used in these experiments, as shown in Fig. 10, yielding approximately 4.36 1Q and 1.51 CZ gates per Clifford depth. This estimation of the CZ-gate error is used for simplicity and we stress that the estimates are subject to the assumption of depolarizing errors and no qubit-subspace leakage [22,30]. The error estimates could be improved by including other experiments (e.g., unitarity benchmarking [64]) but are left for future work.

APPENDIX G: GATE SIMULATOR AND ERROR BUDGET

Based on atomic experiments, we can estimate the contribution of known error sources. We use an approach in which we compute the average fidelity of our CZ gate [48] using a superoperator simulator with measured experimental values as inputs. Errors are averaged over time and represent our understanding of the typical operational state of the machine. This estimation is based on a single gate, rather than a calculation of the fidelity over some specific characterization circuit, i.e., GERB or CRB.

We separate errors between the clock operation and the UV operation. In the clock, we consider six primary error sources: (1) clock-frequency drift, (2) fast laser-frequency noise, (3) trap scattering out of the clock state to the qubit subspace, (4) finite-temperature effects on clock excitation, (5) differential light shift due to the shaped clock pulse between the $|1\rangle$ and $|c\rangle$ states, and (6) loss from the science tweezers. In the UV, we find significant error contributions from (1) the finite Rydberg lifetime, (2) Rydberg decoherence, and (3) pulse repeatability.

During a calibration cycle, the clock frequency drifts. We estimate a Gaussian distributed static detuning with width 33 Hz for the clock operation based on experimental measurements of this frequency drift. Since we use a measurement based on detuning several minutes after calibration, this error source is likely an upper bound for the true error due to this effect. This contributes 0.126% infidelity, with 0.007% of this due to leakage.

The clock laser-frequency noise is estimated based upon a smoothed fit to experimental data of a spin-lock measurement and the implied two-sided phase PSD from exponential decays in the spin-locking experiment shown in Fig. 2(b). This fit goes down to 10 Hz and thus is distinct from the slow-timescale drift. For a given realization of the phase-noise PSD S_ϕ, we sample the laser phase as in Ref. [40]:

$$\phi(t) = 2\sum_k \sqrt{S_\phi(f_k)\Delta f_k}\cos(2\pi f_k t + \phi_k)\,, \qquad \text{(G1)}$$

with ϕ_k chosen randomly and Δf some small step in frequency space. This phase simply adds to the desired phase of the pulses. The clock phase noise contributes 0.116% to the infidelity and 0.088% to the leakage rate.

In order to model the effects of atom temperature on the clock-shelving fraction, we consider only the modification to the resonant carrier Rabi rate due to the Debye-Waller effect. Here, the Rabi rate for the nth motional eigenstate along the direction of the driving laser is reduced by $e^{-\eta^2/2}L_n(\eta^2)$, with $\eta \approx 0.26$ the Lamb-Dicke parameter

and L_n the nth Laguerre polynomial. In order to approximate the pulse-area calibration procedure that takes place at this same temperature, we set the thermally average Rabi rate to give a perfect pulse area for the given pulse duration. Thus, colder than average atoms will be over-rotated while warmer than average atoms will be under-rotated. We choose $\bar{n} = 0.25$ and sample the motional eigenstate independently for both atoms. Temperature effects in the clock cause 0.013% infidelity entirely in the form of leakage.

Raman scattering of off-resonant trap light from the clock state is a known error source. In our nominal traps, the clock state has a lifetime of 1.06 s. In order to simplify the analysis here, we model the leakage scattering as having a branching ratio of 50% to each atomic ground state, since the lifetime of the main intermediate state $^3P_1$ in the decay pathway is short compared to the clock Rabi rate. This contributes 0.019% to infidelity, with 0.008% leaking back to the clock state. The observed 5-s $1/e$ atom loss contributes to 0.005% leakage.

Additionally, due to the ac-Stark shifts from far off-resonant states, the clock operation shifts the differential frequency between $|1\rangle$ and $|c\rangle$ by an average of 125 Hz over the course of the clock pulse. We calibrate the detuning so that the time-averaged detuning is 0, but the light shift varies over the course of the pulse and the shaped clock pulse will only be resonant at its average Rabi rate. This contributes 0.009% error, entirely as leakage since the average detuning is 0.

Turning to UV errors, we model the Rydberg lifetime as 65 μs, where an atom lost from the Rydberg state is assumed to be permanently lost. This leads to a loss probability of 0.075% per pair during the CZ gate. Assuming the measured T_2^* results from quasistatic detuning errors, the root-mean-square (rms) detuning can be calculated as $2\pi \times \Delta_{\mathrm{rms}} = 1/T_2^*$. Simulation of the time-optimal gate with a static detuning error yields an infidelity $2.9(2\pi\Delta/\Omega)^2$, for a total infidelity $2.9/(T_2^*\Omega)^2 = 0.007\%$. Similarly,we expect a small coherent population left in the Rydberg state, that we treat as loss, which contributes 0.001% to such error. We measure atom loss of 0.11(3)% and 0.09(1)% for GERB and CRB after accounting for clock loss (see Table I). The small discrepancy between the predictions of our model and RB measurements can potentially be explained by gate-parameter drift or excess decay of the entangled Rydberg state.

We additionally model a 0.4% variation in the time-optimal pulse area, which is constant over the duration of the UV gate as measured in the experiment. This contributes error at 0.007%, mostly due to the 0.005% loss.

In general, when calculating the fidelity for an arbitrary CZ gate, we are free to choose a single-qubit phase as we see fit. We choose the single-qubit phase that minimizes each error independently, in order to avoid over-estimating coherent errors. We finally recalibrate the parameters of the time-optimal gate for our finite Rydberg blockade of 160 MHz.

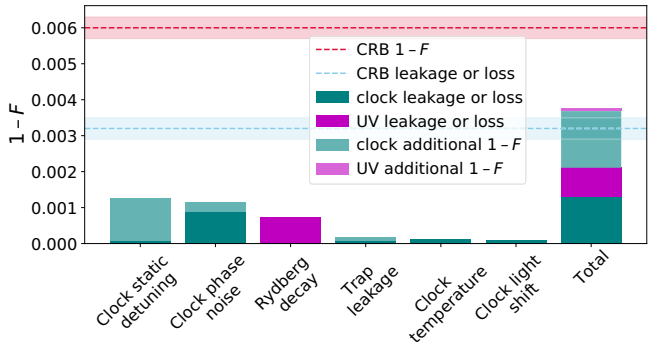

FIG. 11. The error budget based on simulation and analytic calculations. The darker-shaded region in each bar represents the portion of infidelity due to leakage and loss. We include our best understanding of all input error sources from *ab initio* experimental measurements.

We summarize the contributions of each error source with $1 - F > 10^{-4}$ in Fig. 11 and also in Table II. In the figure, the height of each bar represents the decrease in average gate fidelity due to this error. The darker portion of the bar gives the probability for either atom to be outside of the qubit subspace following the CZ gate, i.e., at least one atom is either leaked or lost. The lighter portion alone is the portion of the error not due to leakage or loss. The bars are colored according to whether they occur on the clock operation (green) or the UV operation (magenta). Along with these error sources, we show the experimentally measured CZ CRB and GERB infidelities, as well as the numerically modeled totals for both leakage and loss, and the decrease in fidelity ΔF. This error budget predicts an infidelity of 0.375% with at least one atom leaked or lost 0.211% of the time.

When realizing a CZ-GERB experiment, effects such as single-qubit phase errors are not relevant due to the global echo present in each GERB block. Therefore, we expect

TABLE II. A summary of the simulated error sources in our CZ gate, as compared to Fig. 11.

Error source	Infidelity (%)	Leakage or loss (%)
Clock static detuning	0.126	0.007
Clock phase noise	0.116	0.088
Clock temperature	0.013	0.013
Clock scattering	0.019	0.008
Clock loss	0.005	0.005
Clock light shift	0.009	0.009
UV T_1	0.075	0.075
UV T_2^*	0.007	0.001
UV repeatability	0.007	0.005
Totals	0.375	0.211

most of the CZ-GERB error to be caused by leakage, loss, and any gate-parameter calibration errors. For other metrics such as the Clifford RB ones, additional errors that are not echoed—e.g., those that affect the single-qubit phase—contribute to the measurement.

Regarding the disagreement between the simulated error budget and experimentally measured errors, we have identified some potential error sources that will be subjected to further investigation. We have declined to include errors in the error budget that are not experimentally well characterized. For example, we have observed an approximately 30% larger clock leakage and loss than what we expected due to clock-related errors, which are transferred into the CZ gate. We have also observed larger loss than predicted by the single-atom Rydberg T_1 measurements with the 460-nm traps on during the measurement, but the Rydberg T_2 and T_2^* measurements are fully explained by the UV laser-frequency noise. Although, experimentally, the time between consecutive CZ gates is always much larger than the Rydberg T_1, the dynamics of these populations over long circuits are also not considered in this gate simulator, which could impact deeper circuits.

We know of other potential effects that can contribute to this error budget. Some are relatively small, i.e., clock laser-intensity noise, Doppler effects, and finite Rydberg blockade. However, other effects are less well known—e.g., the effect of atom motion in an imperfect trapping potential when probed by a Doppler-sensitive operation such as our clock shelving—and a complete understanding of how Rydberg pair states affect the CZ gate under practical operational conditions that involve multiple lasers and background fields. Future work will investigate the impact of these additional effects on our CZ gates.

[1] A. M. Stephens, Fault-tolerant thresholds for quantum error correction with the surface code, Phys. Rev. A **89**, 022321 (2014).

[2] M. Norcia, *et al.*, Iterative assembly of ^{171}Yb atom arrays with cavity-enhanced optical lattices, PRX Quantum **5**, 030316 (2024).

[3] G. Pichard, D. Lim, E. Bloch, J. Vaneecloo, L. Bourachot, G.-J. Both, G. Mériaux, S. Dutartre, R. Hostein, J. Paris, B. Ximenez, A. Signoles, A. Browaeys, T. Lahaye, and D. Dreon, Rearrangement of individual atoms in a 2000-site optical-tweezer array at cryogenic temperatures, Phys. Rev. Appl. **22**, 024073 (2024).

[4] H. J. Manetsch, G. Nomura, E. Bataille, K. H. Leung, X. Lv, and M. Endres, A tweezer array with 6100 highly coherent atomic qubits, ArXiv:2403.12021.

[5] K. Singh, C. Bradley, S. Anand, V. Ramesh, R. White, and H. Bernien, Mid-circuit correction of correlated phase errors using an array of spectator qubits, Science **380**, 1265 (2023).

[6] E. Deist, Y.-H. Lu, J. Ho, M. K. Pasha, J. Zeiher, Z. Yan, and D. M. Stamper-Kurn, Mid-circuit cavity measurement in a neutral atom array, Phys. Rev. Lett. **129**, 203602 (2022).

[7] T. M. Graham, L. Phuttitarn, R. Chinnarasu, Y. Song, C. Poole, K. Jooya, J. Scott, A. Scott, P. Eichler, and M. Saffman, Mid-circuit measurements on a single-species neutral alkali atom quantum processor, Phys. Rev. X **13**, 041051 (2023).

[8] M. A. Norcia, *et al.*, Mid-circuit qubit measurement and rearrangement in a ^{171}Yb atomic array, Phys. Rev. X **13**, 041034 (2023).

[9] J. W. Lis, A. Senoo, W. F. McGrew, F. Rönchen, A. Jenkins, and A. M. Kaufman, Mid-circuit operations using the *omg* architecture in neutral atom arrays, Phys. Rev. X **13**, 041035 (2023).

[10] D. Bluvstein, *et al.*, Logical quantum processor based on reconfigurable atom arrays, Nature **626**, 58 (2024).

[11] K. Barnes, *et al.*, Assembly and coherent control of a register of nuclear spin qubits, Nat. Commun. **13**, 2779 (2022).

[12] H. Levine, A. Keesling, G. Semeghini, A. Omran, T. T. Wang, S. Ebadi, H. Bernien, M. Greiner, V. Vuletić, H. Pichler, and M. D. Lukin, Parallel implementation of high-fidelity multiqubit gates with neutral atoms, Phys. Rev. Lett. **123**, 170503 (2019).

[13] S. J. Evered, D. Bluvstein, M. Kalinowski, S. Ebadi, T. Manovitz, H. Zhou, S. H. Li, A. A. Geim, T. T. Wang, N. Maskara, H. Levine, G. Semeghini, M. Greiner, V. Vuletić, and M. D. Lukin, High-fidelity parallel entangling gates on a neutral-atom quantum computer, Nature **622**, 268 (2023).

[14] I. S. Madjarov, J. P. Covey, A. L. Shaw, J. Choi, A. Kale, A. Cooper, H. Pichler, V. Schkolnik, J. R. Williams, and M. Endres, High-fidelity entanglement and detection of alkaline-earth Rydberg atoms, Nat. Phys. **16**, 857 (2020).

[15] M. Peper, Y. Li, D. Y. Knapp, M. Bileska, S. Ma, G. Liu, P. Peng, B. Zhang, S. P. Horvath, A. P. Burgers, and J. D. Thompson, Spectroscopy and modeling of ^{171}Yb Rydberg states for high-fidelity two-qubit gates, Phys. Rev. X **15**, 011009 (2025).

[16] A. Jenkins, J. W. Lis, A. Senoo, W. F. McGrew, and A. M. Kaufman, Ytterbium nuclear-spin qubits in an optical tweezer array, Phys. Rev. X **12**, 021027 (2022).

[17] Q. Xu, J. P. Bonilla Ataides, C. A. Pattison, N. Raveendran, D. Bluvstein, J. Wurtz, B. Vasić, M. D. Lukin, L. Jiang, and H. Zhou, Constant-overhead fault-tolerant quantum computation with reconfigurable atom arrays, Nat. Phys. **20**, 1084 (2024).

[18] Y. Hong, M. Marinelli, A. M. Kaufman, and A. Lucas, Long-range-enhanced surface codes, Phys. Rev. A **110**, 022607 (2024).

[19] J. I. Cirac and P. Zoller, Quantum computations with cold trapped ions, Phys. Rev. Lett. **74**, 4091 (1995).

[20] A. Sørensen and K. Mølmer, Quantum computation with ions in thermal motion, Phys. Rev. Lett. **82**, 1971 (1999).

[21] E. Urban, T. A. Johnson, T. Henage, L. Isenhower, D. D. Yavuz, T. G. Walker, and M. Saffman, Observation of Rydberg blockade between two atoms, Nat. Phys. **5**, 110 (2009).

[22] C. H. Baldwin, B. J. Bjork, J. P. Gaebler, D. Hayes, and D. Stack, Subspace benchmarking high-fidelity entangling operations with trapped ions, Phys. Rev. Res. **2**, 013317 (2020).

[23] R. B.-S. Tsai, X. Sun, A. L. Shaw, R. Finkelstein, and M. Endres, Benchmarking and fidelity response theory of high-fidelity Rydberg entangling gates, PRX Quantum **6**, 010331 (2025).

[24] J. Emerson, R. Alicki, and K. Życzkowski, Scalable noise estimation with random unitary operators, J. Opt. B: Quantum Semiclassical Opt. **7**, S347 (2005).

[25] C. Dankert, R. Cleve, J. Emerson, and E. Livine, Exact and approximate unitary 2-designs and their application to fidelity estimation, Phys. Rev. A **80**, 012304 (2009).

[26] B. W. Reichardt, *et al.*, Logical computation demonstrated with a neutral atom quantum processor, ArXiv:2411.11822.

[27] T. O. Höhn, E. Staub, G. Brochier, N. Darkwah Oppong, and M. Aidelsburger, State-dependent potentials for the $^1S_0$ and $^3P_0$ clock states of neutral ytterbium atoms, Phys. Rev. A **108**, 053325 (2023).

[28] D. C. McKay, C. J. Wood, S. Sheldon, J. M. Chow, and J. M. Gambetta, Efficient Z gates for quantum computing, Phys. Rev. A **96**, 022330 (2017).

[29] J. P. Gaebler, A. M. Meier, T. R. Tan, R. Bowler, Y. Lin, D. Hanneke, J. D. Jost, J. P. Home, E. Knill, D. Leibfried, and D. J. Wineland, Randomized benchmarking of multiqubit gates, Phys. Rev. Lett. **108**, 260503 (2012).

[30] E. Magesan, J. M. Gambetta, and J. Emerson, Scalable and robust randomized benchmarking of quantum processes, Phys. Rev. Lett. **106**, 180504 (2011).

[31] E. Magesan, J. M. Gambetta, and J. Emerson, Characterizing quantum gates via randomized benchmarking, Phys. Rev. A **85**, 042311 (2012).

[32] S. Kimmel, G. H. Low, and T. J. Yoder, Robust calibration of a universal single-qubit gate set via robust phase estimation, Phys. Rev. A **92**, 062315 (2015).

[33] T. Wilk, A. Gaëtan, C. Evellin, J. Wolters, Y. Miroshnychenko, P. Grangier, and A. Browaeys, Entanglement of two individual neutral atoms using Rydberg blockade, Phys. Rev. Lett. **104**, 010502 (2010).

[34] T. M. Graham, M. Kwon, B. Grinkemeyer, Z. Marra, X. Jiang, M. T. Lichtman, Y. Sun, M. Ebert, and M. Saffman, Rydberg-mediated entanglement in a two-dimensional neutral atom qubit array, Phys. Rev. Lett. **123**, 230501 (2019).

[35] S. Ma, A. P. Burgers, G. Liu, J. Wilson, B. Zhang, and J. D. Thompson, Universal gate operations on nuclear spin qubits in an optical tweezer array of ^{171}Yb atoms, Phys. Rev. X **12**, 021028 (2022).

[36] D. Jaksch, J. I. Cirac, P. Zoller, S. L. Rolston, R. Côté, and M. D. Lukin, Fast quantum gates for neutral atoms, Phys. Rev. Lett. **85**, 2208 (2000).

[37] D. J. Wineland and W. M. Itano, Laser cooling of atoms, Phys. Rev. A **20**, 1521 (1979).

[38] R. Finkelstein, R. B.-S. Tsai, X. Sun, P. Scholl, S. Direkci, T. Gefen, J. Choi, A. L. Shaw, and M. Endres, Universal quantum operations and ancilla-based read-out for tweezer clocks, Nature **634**, 321 (2024).

[39] H. Ball, W. D. Oliver, and M. J. Biercuk, The role of master clock stability in quantum information processing, npj Quantum Inf. **2**, 1 (2016).

[40] X. Jiang, J. Scott, M. Friesen, and M. Saffman, Sensitivity of quantum gate fidelity to laser phase and intensity noise, Phys. Rev. A **107**, 042611 (2023).

[41] S. Dörscher, R. Schwarz, A. Al-Masoudi, S. Falke, U. Sterr, and C. Lisdat, Lattice-induced photon scattering in an optical lattice clock, Phys. Rev. A **97**, 063419 (2018).

[42] D. Wineland, C. Monroe, W. Itano, D. Leibfried, B. King, and D. Meekhof, Experimental issues in coherent quantum-state manipulation of trapped atomic ions, J. Res. Natl. Inst. Stand. Technol. **103**, 259 (1998).

[43] M. H. Levitt, Composite pulses, Prog. Nucl. Magn. Reson. Spectrosc. **18**, 61 (1986).

[44] M. H. Levitt and R. Freeman, NMR population inversion using a composite pulse, J. Magn. Reson. **33**, 473 (1979).

[45] F. Kéfélian, H. Jiang, P. Lemonde, and G. Santarelli, Ultralow-frequency-noise stabilization of a laser by locking to an optical fiber-delay line, Opt. Lett. **34**, 914 (2009).

[46] M. Saffman, Quantum computing with atomic qubits and Rydberg interactions: Progress and challenges, J. Phys. B: At., Mol. Opt. Phys. **49**, 202001 (2016).

[47] J. T. Wilson, S. Saskin, Y. Meng, S. Ma, R. Dilip, A. P. Burgers, and J. D. Thompson, Trapping alkaline earth Rydberg atoms optical tweezer arrays, Phys. Rev. Lett. **128**, 033201 (2022).

[48] S. Jandura and G. Pupillo, Time-optimal two-and three-qubit gates for Rydberg atoms, Quantum **6**, 712 (2022).

[49] K. Sahay, J. Jin, J. Claes, J. D. Thompson, and S. Puri, High-threshold codes for neutral-atom qubits with biased erasure errors, Phys. Rev. X **13**, 041013 (2023).

[50] D. Gottesman, An introduction to quantum error correction and fault-tolerant quantum computation, ArXiv:0904.2557.

[51] J. P. Gaebler, A. M. Meier, T. R. Tan, R. Bowler, Y. Lin, D. Hanneke, J. D. Jost, J. P. Home, E. Knill, D. Leibfried, and D. J. Wineland, Randomized benchmarking of multiqubit gates, Phys. Rev. Lett. **108**, 260503 (2012).

[52] S. Ma, G. Liu, P. Peng, B. Zhang, S. Jandura, J. Claes, A. P. Burgers, G. Pupillo, S. Puri, and J. D. Thompson, High-fidelity gates and mid-circuit erasure conversion in an atomic qubit, Nature **622**, 279 (2023).

[53] A. Javadi-Abhari, M. Treinish, K. Krsulich, C. J. Wood, J. Lishman, J. Gacon, S. Martiel, P. D. Nation, L. S. Bishop, A. W. Cross, *et al.*, Quantum computing with QISKIT, ArXiv:2405.08810.

[54] D. Bluvstein, H. Levine, G. Semeghini, T. T. Wang, S. Ebadi, M. Kalinowski, A. Keesling, N. Maskara, H. Pichler, M. Greiner, *et al.*, A quantum processor based on coherent transport of entangled atom arrays, Nature **604**, 451 (2022).

[55] L. Li, W. Huie, N. Chen, B. DeMarco, and J. P. Covey, Active cancellation of servo-induced noise on stabilized lasers via feedforward, Phys. Rev. Appl. **18**, 064005 (2022).

[56] F. Hummel, S. Weber, J. Mögerle, H. Menke, J. King, B. Bloom, S. Hofferberth, and M. Li, Engineering Rydberg-pair interactions in divalent atoms with hyperfine-split ionization thresholds, Phys. Rev. A **110**, 042821 (2024).

[57] H. Bombín, Single-shot fault-tolerant quantum error correction, Phys. Rev. X **5**, 031043 (2015).

[58] F. Nogrette, H. Labuhn, S. Ravets, D. Barredo, L. Béguin, A. Vernier, T. Lahaye, and A. Browaeys, Single-atom trapping in holographic 2D arrays of microtraps with arbitrary geometries, Phys. Rev. X **4**, 021034 (2014).

[59] S. Ahn, K. Park, D. Cho, M. Lim, T. Choi, and A. S. Moskalenko, Single-qubit quantum gate at an arbitrary speed, ArXiv:2412.19561.

[60] D. A. Rower, L. Ding, H. Zhang, M. Hays, J. An, P. M. Harrington, I. T. Rosen, J. M. Gertler, T. M. Hazard, B. M. Niedzielski, *et al.*, Suppressing counter-rotating errors for fast single-qubit gates with fluxonium, PRX Quantum **5**, 040342 (2024).

[61] L.-S. Ma, P. Jungner, J. Ye, and J. L. Hall, Delivering the same optical frequency at two places: Accurate cancellation of phase noise introduced by an optical fiber or other time-varying path, Opt. Lett. **19**, 1777 (1994).

[62] N. Lambert, E. Giguère, P. Menczel, B. Li, P. Hopf, G. Suárez, M. Gali, J. Lishman, R. Gadhvi, R. Agarwal, *et al.*, QuTiP 5: The quantum toolbox in PYTHON, ArXiv:2412.04705.

[63] L. H. Pedersen, N. M. Møller, and K. Mølmer, Fidelity of quantum operations, Phys. Lett. A **367**, 47 (2007).

[64] A. Carignan-Dugas, J. J. Wallman, and J. Emerson, Bounding the average gate fidelity of composite channels using the unitarity, New J. Phys. **21**, 053016 (2019).